From Classical to Quantum Dynamics of Atomic and Ionic Species Interacting with Graphene and Its Analogue *

Sophya Garashchuk[1], Jingsong Huang[2,3], Bobby G. Sumpter[2,3], and Jacek Jakowski[†2,3]

[1] *Department of Chemistry & Biochemistry, University of South Carolina, Columbia, SC 29208*

[2] *Center for Nanophase Materials Sciences, Oak Ridge National Laboratory, Oak Ridge, TN 37831*

[3] *Computational Sciences & Engineering Division, Oak Ridge National Laboratory, Oak Ridge, TN 37831*

May 25, 2020

Abstract

Graphene and its analogues offer a broad range of application opportunities for (opto)-electronics, sensing, catalysis, phase separation, energy conversion and storage, etc. Engineering graphene properties often relies on its controllable functionalization, defect formation and patterning, and reactive gas etching. In this chapter, we survey the dynamics of graphene using classical and quantum-classical dynamics methods. We discuss the reactivity, scattering, and transmission of atomic and ionic species including Ar cluster ion, H/D, and H^+/D^+ on graphene flakes of various sizes, focusing on the atomic-scale motion and energy dissipation pathways involved in forming and breaking covalent bonding. Discussions on the nuclear quantum effects of light species, the effects of isotopic substitution, and the methodologies for such modeling are also included.

Keywords: Beam-Matter Interactions, Bohmian Dynamics, Density Functional Tight Binding, Nuclear Quantum Effects, Quantum Trajectories

[†]jakowskij@ornl.gov

1 Introduction

Understanding interactions and chemical activities of graphene and its two-dimensional layered analogues with small molecules or ions offers a broad range of opportunities for designing novel applications such as nanoscale (opto)-electronics, few-particle sensors, catalysis, membranes for efficient gas and liquid sieving, phase separation, energy conversion and storage, and quantum information devices [1]. The semiconducting properties of graphene nanoribbons and hexagonal boron nitride (hBN) nanoribbons are known to depend on their width and edge character [2, 3, 4, 5]. Further tailoring of their opto-electronic properties can be achieved by employing physico-chemical processes and interactions that alter the number of π-conjugated electrons. Even a single vacancy deformation or interaction with a small number of molecules that chemically engage graphene's π-conjugated orbitals can have measurable effects [6, 7, 8, 9]. Toward engineering the properties of these materials for desired applications, techniques based on focused ion and electron beams have been demonstrated as effective tools for cleaning, cutting, etching, patterning, and controllable defect formation. Possible defects include Stone-Wales type transformation, lattice dislocations, formation of vacancies and nanopores, substitution of carbon with other atoms, as well as chemical functionalization that transforms sp^2 hybridized carbon atoms into sp^3 centers [1]. To gain fundamental understandings of beam-matter interactions, it is indispensable to conduct multiscale and multiphysics modeling of relevant physico-chemical processes on realistic time scales and molecular system sizes.

In this chapter we survey the approaches for first-principles dynamics modeling of the interactions between graphene and beams of atomic and ionic species. Methods for ab initio dynamics focusing on nuclear motion (classical and quantum) of graphene and beam species on the ground electronic state are discussed. We begin by sketching a theory of time-dependent field separation as a starting point for a multiscale and multiphysics decomposition of large molecular systems into fragments that are treatable with different theoretical approaches. A quantum trajectory method is then discussed as an approach for treating nuclear quantum effects (NQEs) for selected light nuclei. The density functional tight binding (DFTB) theory, which is an inexpensive, approximate density functional theory (DFT) used in conjunction with a quantum trajectory, is also outlined. We do not include the effects of beam induced electronic excitation and dynamics on the excited states surfaces, which are addressed separately in Chapter 8 of this book. Following the review of theory we present a few examples of simulations that illustrate a range of physico-chemical phenomena caused by interactions between beam and graphene and related computational aspects. We discuss reactivity, scattering, and transmission of atomic and ionic species including Ar cluster ion, H/D, and H^+/D^+ on graphene, focusing on the atomic-scale motion and energy dissipation pathways involved in forming and breaking covalent bonding, the NQEs for light species, and the isotopic

substitution effects.

2 Theoretical Methods

Today's fabrication and processing of advanced materials are increasingly complex with technological applications heading towards the quantum scale and involving simultaneous manipulation of atoms, electrons, and light (photons). The multiscale and multiphysics character of physics and chemistry behind processes related to fabrication and functioning of such materials often requires computational techniques and methods capable of spanning across several scales of time and space. Multiscale modeling of physico-chemical processes on realistic time scales and molecular system sizes often involves partitioning the system into active and inactive (spectator) parts, which can be treated at different levels of theory. Such partitioning can be achieved via time-dependent field separation. Typically for ab initio dynamics modeling of irradiation processes, the inexpensive electronic structure methods are desired such as DFTB theory.

2.1 Multiphysics modeling

There is a wide range of excellent computational chemistry tools that focus on a specific science aspect but neglect other less important parts of the big picture (e.g., the multiphysics). A comprehensive review of dynamics methods/approaches is difficult to achieve in a finite space, so we limit this discussion to representative methods and selected references. A typical approach focuses on one specific aspect (for example the evolution of electrons) while using a simplest possible (and computationally cheap) theoretical framework for the rest of the species. Figure 1 illustrates a multiscale partitioning of H adsorption on graphene for multiphysics treatment on different scales.

For the nuclei, conventional molecular dynamics approaches provide an appropriate description of nuclear dynamics as classical particles in many situations [10, 11]. However, for understanding of chemical processes at low energy or temperature, it is essential to include the quantum-mechanical (**QM**) effects, such as the zero-point energy (**ZPE**), tunneling and nonadiabatic transitions, even in large molecular systems or in condensed phases. For example, QM tunneling is known to dominate proton transfer at low temperature in biological environments. In the area of bond-selective chemistry, the intermode energy flow and the ZPE should be considered for understanding effects of the vibrational excitation on bond breaking. Incorporation of the QM effects into classical trajectory simulation is desirable when describing chemical reactions in large molecular systems. Fully quantum approaches to the time-dependent Schrödinger equation (TDSE), based on a direct product Finite Basis or Discrete Variable representations, are difficult to extend beyond 10-12 degrees of freedom

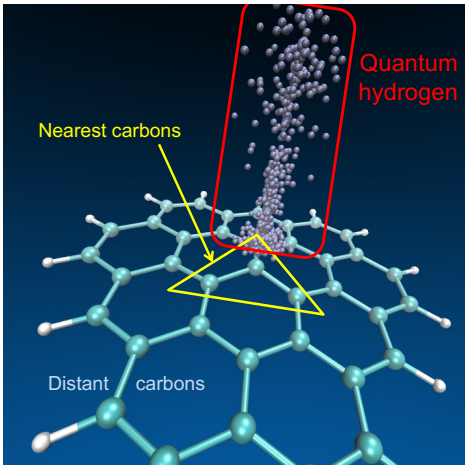

Figure 1: An example of hierarchical multiscale partitioning for multiphysics treatment of nuclear motion for the adsorption of H irradiated on graphene. Fully quantum hydrogen is represented as an ensemble of quantum trajectories (purple spheres). Nearest carbons to the adsorption site marked by the yellow triangle can be treated using classical molecular dynamics. Distant, edge carbons are treated as frozen or via a force field.

due to the exponential scaling of computational cost [12, 13]. To achieve improved scalability, one can express the nuclear wavefunction in terms of optimized basis functions. Such an approach is used in the Multi-Configurational Time-Dependent Hartree (MCTDH) methods, multiple spawning, coupled and local coherent states approximation and split operator Fourier transform based approaches [14, 15, 16, 17, 18, 19, 20, 21]. Nevertheless, even with improved scaling the computational cost is still a limitation for large scale system applications. Therefore, mixed approaches, in which a selected small number of degrees of freedom are treated quantum mechanically while the remaining nuclei are treated classically, are computationally very attractive [22, 23, 24, 25, 26, 27]. Among other approaches are Semiclassical Initial Value Representation, Quasiclassical Trajectory Dynamics, Centroid Molecular Dynamics, Ring Polymer Molecular Dynamics and Path Integral Molecular Dynamics [28, 29, 30, 31, 32].

For the electrons, one can either solve the stationary time-independent electronic structure problem, which leads to Born-Oppenheimer molecular dynamics. Alternatively, one directly integrates the time-dependent Schrödinger or Kohn-Sham DFT equations. The two most widely used classes of first-principles molecular dynamics (MD) with time-dependent quantum mechanical treatment of the electrons are Ehrenfest dynamics and surface hopping dynamics, each having its own limitations. Ehrenfest dynamics offers correct short-term behavior of coherent evolution of the superposition of electronic states in the strong coupling region but the long-time trajectory follows an incorrect averaged state trajectory. The surface hopping approaches are based on stochastic branching of

trajectories to recover a correct long-time behavior. In a fully quantum description for all nuclei and electrons the correct approach should retain features of both approaches – coherent mean-field mixing of electronic states in the strong coupling region and the ability of a wavefunction to split into spatially separated branches precluding possibility for interference. These features could be included into mean-field approaches by adding a coherence dephasing term that switches the electronic surfaces during the dynamics [33, 34, 35, 36].

2.2 Multiscale separation within the time-dependent mean-field approximation

The separation of electronic degrees of freedom from those describing heavy classical nuclei and light quantum nuclei can be formally achieved through the time-dependent self-consistent field. An outline of the derivation, using one-dimensional notations, is presented below. The mass of an electron is equal to one atomic mass unit; M and m denote the mass of the classical and quantum particles, respectively. Taking advantage of the mass- and time-scale separation, the following wavefunction ansatz is used

$$\Phi\left(r_e, x, R, t\right) \approx \phi\left(r_e, t; x(t), R(t)\right) \cdot \psi(x, t; R(t)) \cdot \chi\left(R, t\right) \cdot \exp\left(-\frac{\imath}{\hbar}\int_0^t E\left(\tau\right) d\tau\right), \tag{1}$$

where r_e, x and R describe, respectively, the electrons, the light quantum nuclei, and the heavy (quasi)classical nuclei. The wavefunctions depend parametrically on the variables after the semicolon. Inserting this ansatz into the time-dependent Schrödinger equation

$$\imath\hbar\frac{\partial\Phi}{\partial t} = \left\{-\sum_R \frac{\hbar^2}{2M}\Delta_R - \sum_x \frac{\hbar^2}{2m}\Delta_x - \sum_{r_e}\frac{\hbar^2}{2}\Delta_{r_e} + \hat{V}_{int}\right\}\Phi, \tag{2}$$

and multiplying on the left by $\langle\chi,\psi|$, $\langle\chi,\phi|$, $\langle\psi,\phi|$, respectively, one obtains the following coupled equations:

$$\imath\hbar\frac{\partial}{\partial t}\phi(r_e, t; x(t), R(t)) = \left\{-\sum_{r_e}\frac{\hbar^2}{2}\Delta_{r_e} + V_{r_e-x,R}\right\}\phi\left(r_e, t; x(t), R(t)\right) \qquad \text{electrons} \tag{3}$$

$$\imath\hbar\frac{\partial}{\partial t}\psi(x, t; R(t)) = \left\{-\sum_x \frac{\hbar^2}{2m}\Delta_x + V_{x-r_e,R}\right\}\psi\left(x, t; R(t)\right) \qquad \text{light quantum nuclei} \tag{4}$$

$$\imath\hbar\frac{\partial}{\partial t}\chi(R, t) = \left\{-\sum_R \frac{\hbar^2}{2M}\Delta_R + V_{R-r_e,x}\right\}\chi\left(R, t\right) \qquad \text{heavy (quasi)classical nuclei} \tag{5}$$

in which the term V_{X-Y} denotes the mean field interaction of particle X with the system Y. The above separation provides the framework for a "modular" implementation of dynamics in which different methods can be applied to different subsystems.

We describe the NQEs for selected light atoms using the Bohmian Quantum Trajectories framework [37]. This approach naturally includes the effect of anharmonicity of the potential energy surface for the nuclei and is very suited for parallelization on Hight Performance Computing (HPC) resources. The wave equation for the quantum nuclei (Eq. (4)) is transformed into a particle trajectory equation by expressing the complex wavefunction $\psi(x,t)$ in terms of the real amplitude and phase, as outlined in Section 2.3. The wavefunction $\psi(x,t)$ is discretized as an ensemble of trajectories such that the probability density of finding a quantum particle in space is given by $|\psi|^2$ and the trajectory momentum is given by the gradient of the wavefunction phase. The time evolution of quantum trajectories unfolds on the potential energy surface, which contains an additional quantum potential $U(x,t)$ besides the classical potential V coming from the electronic structure. That is, the quantum nuclei move according to the combined action of the classical force, $F_{cl} = -\nabla V$, and the quantum force $F_{qm} = -\nabla U$. The quantum potential U describes the non-locality of the nuclear wavefunction. At any given position in space, U depends on the values of the nuclear wavefunction amplitude and on its second derivatives, $U = -\hbar^2\nabla^2|\psi|/(2m|\psi|)$.

For the classical treatment of the heavy nuclei, the time-dependent wavefunction $\chi(R,t)$ is replaced with the classical trajectory whose position and momentum correspond to the expectation values $\langle\chi|R|\chi\rangle \rightarrow R$ and $\langle\chi|-\imath\hbar\frac{\partial}{\partial R}|\chi\rangle \rightarrow P$, respectively. The trajectory momentum is updated according to the force averaged over the probability distribution of the quantum particles according to the Ehrenfest theorem [38]. This is a standard approach underlying ab initio molecular dynamics schemes. For the electrons one can (i) invoke the Born-Oppenheimer approximation and replace the time-dependent electronic wavefunction $\phi\,(r,t)$ solving the TDSE (Eq. (3)) with the ground-state wavefunction, or (ii) directly integrate Eq. (3). In this chapter we assume that the nuclear dynamics follows on the ground electronic state. The procedures for direct integration of the time-dependent electronic structure are presented in Chapter 8. We primarily employ the DFTB theory for description of the electronic structure because of its optimal balance of accuracy and computational cost. Section 2.5 details a brief description of the DFTB theory.

2.3 Quantum trajectory dynamics

The *quantum or Bohmian trajectory* formulation [39] of the TDSE is discussed below, assuming the same mass m for all degrees of freedom (DOFs) described in Cartesian coordinates. A generalization is given in Ref. [40]. Small bold letters denote vectors and capital bold letters denote matrices, whose

dimensionality is N_{dim}. The usual TDSE is then,

$$\hat{H}\psi(\boldsymbol{x},t) = \imath\hbar\frac{\partial}{\partial t}\psi(\boldsymbol{x},t), \quad \hat{H} = -\frac{\hbar^2}{2m}\boldsymbol{\nabla}\cdot\boldsymbol{\nabla} + V(\boldsymbol{x}). \tag{6}$$

Using the polar form of the wavefunction (the amplitude $A(\boldsymbol{x},t)$ and the phase $S(\boldsymbol{x},t)$ are real functions),

$$\psi(\boldsymbol{x},t) = A(\boldsymbol{x},t)\exp\left(\frac{\imath}{\hbar}S(\boldsymbol{x},t)\right), \tag{7}$$

and defining the classical ($\boldsymbol{p}$) and the non-classical ($\boldsymbol{r}$) momentum components,

$$\boldsymbol{p} := \boldsymbol{\nabla}S, \quad \boldsymbol{r} := \frac{\boldsymbol{\nabla}A}{A} \tag{8}$$

the TDSE leads to the following equations of motion for a trajectory described by the associated quantities $(\boldsymbol{x}_t, \boldsymbol{p}_t, \boldsymbol{r}_t, S_t)$:

$$\frac{d\boldsymbol{x}_t}{dt} = \frac{\boldsymbol{p}_t}{m} \tag{9}$$

$$\frac{d\boldsymbol{p}_t}{dt} = -\boldsymbol{\nabla}\left.(V+U)\right|_{\boldsymbol{x}=\boldsymbol{x}_t} \tag{10}$$

$$\frac{d\boldsymbol{r}_t}{dt} = -\left(\boldsymbol{r}_t\cdot\boldsymbol{\nabla} + \frac{\boldsymbol{\nabla}\cdot\boldsymbol{\nabla}}{2}\right)\frac{\boldsymbol{p}_t}{m} \tag{11}$$

$$\frac{dS_t}{dt} = \frac{\boldsymbol{p}_t\cdot\boldsymbol{p}_t}{2m} - \left.(V+U)\right|_{\boldsymbol{x}=\boldsymbol{x}_t}. \tag{12}$$

The subscript t labels attributes of the quantum trajectories (**QT**s), which discretize the initial wavefunction and, as an ensemble, represent $\psi(\boldsymbol{x},t)$ at all times. The quantum-mechanical features of dynamics enter these classical-like equations of motion via the quantum potential U, expressed in terms of $\boldsymbol{r}$ as,

$$U(\boldsymbol{x},t) = -\frac{\hbar^2}{2m}(\boldsymbol{r}\cdot\boldsymbol{r} + \boldsymbol{\nabla}\cdot\boldsymbol{r}). \tag{13}$$

The quantum potential is non-local in $\boldsymbol{x}$ and, being proportional to $\hbar^2/m$, suggests a simple formal transition to classical mechanics: $U \to 0$. (The atomic units of $\hbar = 1$ are used henceforth.) The trajectory weight w_t, which is the probability density within the volume element associated with each QT, $\delta\boldsymbol{x}_t = \delta x_1 \cdot \delta x_2 \ldots \delta x_{N_{dim}}$, is conserved in time [41],

$$w_t = |\psi(\boldsymbol{x}_0)|^2\delta\boldsymbol{x}_0 = |\psi(\boldsymbol{x}_t)|^2\delta\boldsymbol{x}_t. \tag{14}$$

Thus, the expectation values of position-dependent operators $\hat{O}$ are readily computed as a sum over all QTs, their number being N_{traj}:

$$\langle \hat{O} \rangle = \int |\psi(\boldsymbol{x},t)|^2 O(\boldsymbol{x}) d\boldsymbol{x} = \sum_{k=1}^{N_{traj}} O(\boldsymbol{x}_t^{(k)}) w^{(k)}. \tag{15}$$

The expectation values are used to analyze dynamics and, also, to construct approximations to the quantum potential U [41, 42] necessary to keep the approach practical [43].

2.4 Approximations to the quantum force

The QM effects in the QT formulation come from the action of the quantum potential U, which is generally singular and reflects the complexity of the time-dependent wavefunction. In the context of nuclear dynamics, however, the mean-field type approximations to the quantum potential are often useful and cost-efficient [41]. For example, for a Gaussian wavefunction, the components of $\boldsymbol{r}$ are linear functions of $\boldsymbol{x}$, U is quadratic and the quantum force is linear in $\boldsymbol{x}$. The 'linearized' quantum force (LQF) can be defined variationally (once integration by parts is used) by the Least Squares Fit [44] of the components of $\boldsymbol{r}$, i. e., by the minimization of a functional I,

$$I = \sum_{\alpha} \langle \| (A^{-1} \boldsymbol{\nabla} A)_\alpha - \tilde{r}_\alpha \|^2 \rangle. \tag{16}$$

The subscript α labels the components of vectors, or DOFs of the system, $\alpha = 1 \ldots N_{dim}$. The fitting functions $\tilde{r}_\alpha = \sum_i c_{i,\alpha} f_i$ are expansions of the components of the vector $A^{-1}\boldsymbol{\nabla} A$ in a linear basis $\boldsymbol{f}$ of the size $N_{dim}+1$, $\boldsymbol{f} = \{x_1, \ldots, x_{N_{dim}}, 1\}$. Minimization with respect to the expansion coefficients $\{c_i\}$ leads to a single linear matrix equation [41]. Apart from the cost of solving this matrix equation, the numerical cost of the global LQF scheme scales linearly with the systems size N_{dim} and with the number of trajectories. This approximation is used in the study of adsorption of H-atom on graphene model (next section).

The global approximation to the quantum potential can be defined without the explicit knowledge of the non-classical momentum $\boldsymbol{r} = (\nabla A)/A$, by invoking integration by parts in Eq. (16). However, calculation of $\boldsymbol{r}$ along the trajectories according to Eq. (11) enables more accurate spatially semi-local or local approximation schemes [45, 46, 47]. Another option for going beyond the global LQF approximation is to use larger, e.g. quadratic in $\boldsymbol{x}$, basis to fit $\boldsymbol{r}$ and $\boldsymbol{p}$, for specific atoms or subsets of strongly coupled DOFs. Note that even if the fitting basis is non-linear, the LSF procedure itself still reduces to a single linear matrix equation. Yet working with the subsets of the DOFs rather than with all DOFs at once, is necessary for practical reasons of controlling the total

basis size; it is also consistent with the typical view of the condensed-phase chemical processes as involving strongly-coupled primary 'system' modes interacting with the weakly-coupled secondary 'bath' modes representing the molecular environment. The quantum force approximation is, then, generated through the following two-step LSF procedure [48].

(i) The global LQF. We perform the Least-Squares Fit of $\boldsymbol{r}$ and $\boldsymbol{p}$ within the linear basis $\boldsymbol{f}$, i. e. minimize the global (with respect to the DOFs) functionals,

$$I_r = \sum_\alpha \langle \| (r_\alpha - \widetilde{r}_\alpha \|^2 \rangle \qquad\qquad I_p = \sum_\alpha \langle \| (p_\alpha - \widetilde{p}_\alpha \|^2 \rangle. \tag{17}$$

For each DOF r_α and p_α are expanded in the Cartesian coordinates of *all* atoms. This first step is similar to the LQF of Eq. (16) except now we fit the actual values of nonclassical and classical momenta evolved along the trajectories. This step describes the quantum force at the LQF level due to correlation of motion between different nuclei.

(ii) The atom-specific high-order fit. The residual $\boldsymbol{r}$ and $\boldsymbol{p}$ are fitted with the higher order polynomials for a single nucleus at a time, using quadratic or higher order Taylor basis in DOFs describing one specific nucleus at a time. Denoting these fitting functions with the double tilde the nuclear-specific functionals are:

$$I_r^{nucl} = \sum_{\alpha \ nucl} \langle \| (r_\alpha - \widetilde{r}_\alpha - \widetilde{\widetilde{r}}_\alpha \|^2 \rangle \qquad\qquad I_p^{nucl} = \sum_{\alpha \ nucl} \langle \| (p_\alpha - \widetilde{p}_\alpha - \widetilde{\widetilde{p}}_\alpha \|^2 \rangle, \tag{18}$$

The second step adds more flexibility to the approximate quantum potential to account for a non-Gaussian shape of the evolving wavefunction. The Least Squares Fit involves solving a linear matrix equation for the matrix size equal to that of the fitting basis.

2.5 Approximate DFT electronic structure

A major hindrance in the development and application of quantum dynamics is the prohibitive cost of electronic structure calculations and the scaling of the related algorithms. To illustrate this, we note that 4 minutes spent on the single calculation of energy and forces translates into 1 month spent on a 10,000 step trajectory. Therefore it is very important to use inexpensive electronic structure methods that are fast, and yet maintain reliable accuracy. Whereas the conventional DFT methods provide a workhorse for a static electronic structure calculations of hundreds to thousands of atoms, yet their relatively high computational cost makes DFT impractical for routine ab initio dynamics of systems consisting more than a few hundred atoms. Semi-empirical and approximate DFT methods based on tight-binding parametrization become critical for modeling large systems as first recognized

by Godecker [49, 50].

In this regard we discuss one such method called DFTB theory, which is a very promising approach offering broad applicability [51, 52, 53]. Although DFTB is approximately 1000 times more expensive than the classical force fields, it is up to 1000 times cheaper than standard density functional theories. Thus DFTB fills the gap between classical force fields and DFT and is an attractive candidate for direct molecular dynamics simulations of bulk and condensed matter systems.

DFTB is an approximate DFT method in which only valence electrons are treated quantum mechanically while all core electrons and nuclei are approximated via pairwise interatomic repulsive potential E_{rep}

$$E = \sum_i 2 f_i \langle \phi_i | H_{core} | \phi_i \rangle + \sum_{\substack{A,B \\ A \neq B}}^{Atoms} \gamma^{AB} \Delta q^A \Delta q^B + \sum_{A>B}^{Atoms} E_{rep}^{AB} \tag{19}$$

where f_i is an occupation number (typically 0 or 1) and i runs over all molecular orbitals. The first term describes the interaction of valence electrons with core ions (nuclei and core electrons). The second term is responsible for electron-electron interaction. Symbols Δq^A and γ^{AB} are, respectively, a charge at center A and a chemical hardness-based parameter describing electron-electrons interactions between centers A and B, which depends on the interatomic distance. The last term describes the interaction between core ions obtained from a fit. An important feature of DFTB is a correct Coulomb asymptotic behavior for interaction of charged molecules. This is due to the fact that γ^{AB} behaves as $1/R_{AB}$ for large interatomic distances. DFTB also provides an inexpensive tool for the description of low lying excitation. Higher energy electronic excitations are less reliable. This limitation is inherent to the use of a minimal basis set (Slater-type orbitals). In addition, DFTB cannot describe processes involving core electrons. The discussion of techniques for modeling electronic excitation is a subject of the next chapter (Chapter 8).

The above energy expression can be rewritten in the matrix form suitable for high performance implementations

$$E = Tr\left[H_{core} P\right] + \frac{1}{2} Tr\left[G\left(P\right) P\right] + \sum_{A>B}^{Atom} E_{rep}^{AB} \tag{20}$$

Symbol P is a reduced one-electron density matrix obtained from molecular orbitals coefficients C, such that $P = C f C^T$. Here, H_{core} and $G(P)$ are atomic orbitals matrices that describe, respectively, the interaction of electrons with core (H_{core}) and electron-electrons interaction ($G(P)$).

The main reason for the low computational cost of DFTB is due to the fact that (a) only valence electrons are considered while core electrons are neglected, (b) a minimal basis set is used (Slater basis), (c) only two-center (pairwise) integrals are used in the calculations. A consequence of (a) and (b) is that for a given molecular system, all matrices (H,G,P) are 5-10 times smaller than in

DFT. A consequence of (c) is that the cost for the formation of all matrices is significantly lower than in DFT.

The solution to the electronic structure needs to be obtained iteratively due to the dependence of matrix $G(P)$ on the electronic structure itself. For that purpose a diagonalization is typically used. The most expensive part of the DFTB is diagonalization, which for the Self-Consistent-Charge version (SCC-DFTB) has to be performed approximately 10-20 times per evaluation of the energy and forces of systems with wide HOMO-LUMO gap [51, 52]. Typically for a trajectory type simulation of a molecular system consisting of a few hundred atoms, around 80% of the time is spent on the diagonalization (including orbital transformations), while approximately 15 % is spent on the evaluation of forces, and the remaining 5% of time is spent on formation of H_{core}, G and overlap matrices. The overall percentage of time spend on $O(N^3)$ operations becomes even larger with increasing size of molecules. This reflects the fact that the formation of DFTB matrices scales quadratically whereas the diagonalization and BLAS3 operations become more and more dominant due to their cubically scaling computational cost [49].

The combined Quantum Trajectory and Electronic Structure (QTES) based on high throughput implementation of the spin-unpolarized SCC-DFTB with Fermi-Dirac smearing at electronic temperature T_{el} [51, 52, 53, 54, 55] is described in Ref. [56]. The calculations are performed on-the-fly for a few thousand trajectories propagated for a several thousand time-steps. The parallel implementation is based on Open Multi-Processing and Message Passing Interface, with evaluations of V and gradients distributed over several hundred cores, and minimal information passed to the head-node where the trajectory attributes for the entire QT ensemble are updated and the output quantities are computed.

3 Simulations

Depending on the type of particles and its energy, the beam irradiation can lead to different physical effects and therefore have different applications. Focused ion and electron beam techniques have been used to engineer defects, for patterning, surface functionalization, and nanopore fabrication [57, 58, 59, 60, 61, 62]. Ar cluster beams, ionized for electrostatic acceleration, are an efficient sputterer of organic contamination from graphene surface [63, 64, 65]. Beside removal of contamination, the irradiation with Ar cluster ion beams can be utilized to fabricate nanopores but can also lead to rupturing of graphene membranes [61, 62, 63, 66, 67]. Unlike Ar beams, H beams can penetrate, scatter or adsorb on a graphene membrane. The adsorption of H atoms at the graphene surface is known as hydrogenation, which has been shown to modify the reactivity and electronic properties

of graphene [68, 69, 70]. The different behavior of Ar and H beams can be ascribed to their different atomic and ionic sizes. The radius of H atoms is much smaller than that of Ar atoms and thus the ion is much smaller as well. The small size of H and H^+ makes their transmission through graphene possible, leading to much smaller energy barriers, especially in the latter case.

The choice of methodology for description of graphene irradiation depends on the mass and energy of beam particles. Due to their large mass and its chemical inactivity, Ar atoms can be treated as classical particles and the effect of irradiation (interaction) with graphene can be described by employing classical dynamics framework without referring to quantum dynamics machinery. For energetic H atoms, the de Broglie wavelength is short and the classical Newtonian framework is also sufficient to describe its dynamics. For low energy H or H^+ beams, however, NQE are expected to play an important role and thus require quantum treatment [71, 72, 73].

We present below a few examples for simulation of graphene irradiation with Ar and H/D beams of various energies and transmission of H^+/D^+ through graphene to illustrate the modeling techniques discussed earlier. We first discuss the irradiation of graphene by an Ar cluster ion beam. Different mechanisms for Ar interactions with supported and suspended graphene are observed, which can be exploited for removal of contaminations or fabrication of nanopores. We then discuss scattering and interaction of an energetic H beam with graphene, focusing on adsorption, reflection, and transmission phenomena. After that we turn to the low energy regime and focus on modeling adsorption of H/D on a graphene flake. The differences between classical and quantum treatment are discussed to expose the role of NQEs. In the final example the transmission of low energy H^+/D^+ through membranes in a liquid instead of gas phase environment is analyzed and discussed for graphene and its isoelectronic hBN analagoue. As these examples illustrate, employing approximate DFT electronic structure methods such as DFTB, while inexpensive, requires benchmarking against more accurate methods and appropriate adjustments of interaction potentials in the critical interaction regions.

3.1 Processing graphene with an Ar cluster ion beam

An Ar cluster ion beam is a positively charged aggregate of Ar atoms, namely Ar_n^+, where n ranges from a few dozens to several thousands atoms, which can be used for nanoscale processing of material surfaces. The ionized clusters are electrostatically accelerated to tens of keV energy before striking the materials surface. It has been demonstrated that irradiation with an Ar_n^+ beam is an effective tool to remove organic contamination from the graphene surface. The surface of graphene synthesized in chemical vapor deposition followed by post-processing is usually covered with more than a nanometer thick layer of contamination, often from polymethylmethacrylate (PMMA) that is used for transfer

and lifting. The distribution of contamination on a graphene surface is non-uniform and can vary from clean areas to areas covered with ∼10 nm thick contaminants. In general during the irradiation of graphene with Ar_n^+, the sputtering of contaminant and graphene damage can occur concurrently, the latter of which can lead to formation of nanopores [62, 65, 66, 67].

Here we analyze the effect of irradiation of graphene with Ar_n^+ using DFTB based classical molecular dynamics. Two types of graphene samples were modelled: suspended and supported. Both types are considered for nanoscale electronics device applications. The computational model consisted of a 5×5 nm^2 graphene flake with approximately 1000 C atoms and an ion cluster with 100 Ar atoms. For modeling the supported graphene, a second graphene layer was placed underneath in the graphite orientation and was frozen during the MD simulations to mimic the effect of support. For modeling the suspended graphene, only one graphene layer was used, which was frozen on the edges during the MD simulations to mimic the effect of suspension. The dangling bonds of the graphene flake's edges where passivated with H. The computational model consisted of over 2100 atoms in total for supported graphene and about half as many for suspended graphene. Employing DFTB for ab initio molecular dynamics is dictated by a balance between accuracy (electronic structure methods are preferable for description of processes involving bond breaking and formation) and computational cost (MD simulations with DFT for 1000+ atoms are typically too expensive).

The main challenge in the computational simulations of the graphene irradiation with Ar_n^+ is the description of potentials for the cluster and its interaction with the graphene surface. This problem is threefold: (1) The standard sets of Slater-Koster parameters used in DFTB simulations do not include noble gas elements. Thus, any choice of DFTB parameters set requires extending it by including Ar-Ar and Ar-C parameters. (2) The character of Ar-Ar bonding and interaction with graphene is not covalent but weak van der Waals type interactions. As such it is notoriously difficult to model using DFT methods. Resorting to more accurate many-body methods such as coupled clusters for validation or adjustment is desired. (3) The overall positive charge of an Ar_n^+ means that not all Ar atoms in the cluster are "made equal". At least one Ar atom is a cation and needs to be treated differently. Contrary to the Ar-Ar case, the Ar-Ar^+ interaction is two orders of magnitude stronger and is the primarily attractive force that holds the cluster together.

The interaction energy profiles for Ar-Ar and Ar-Ar^+ from different electronic structure methods are shown on Figure 2. Highly accurate and experimentally validated Aziz potential for neutral Ar-Ar dimer is also shown for comparison. The CCSD(T) potential for Ar-Ar shows a binding energy amounting to 0.011 eV at 3.8 Å separation and agrees very well with the spectroscopic Aziz potential [74, 75, 76] as excepted. Also with CCSD(T), the binding energy for Ar-Ar^+ amounts to 1.26 eV at interatomic separation of 2.4 Å. Interestingly, the binding energy by CAM-B3LYP with dispersion

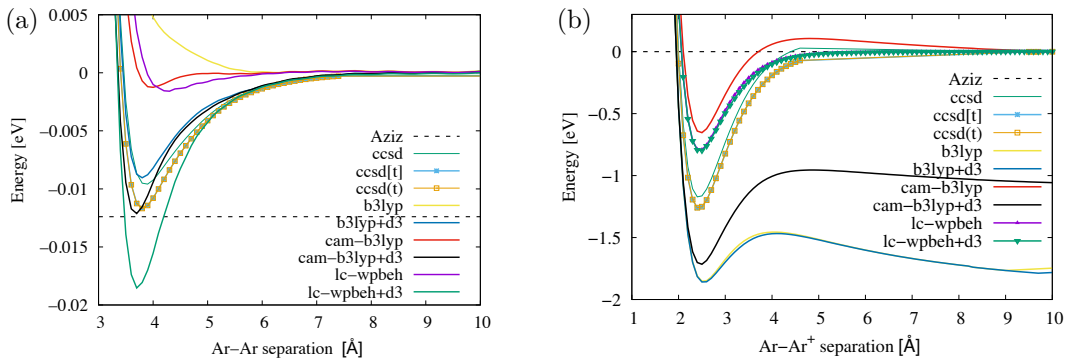

Figure 2: Interaction energy of neutral Ar-Ar (a) and cationic Ar-Ar$^+$ (b) as a function of interatomic separation from different electronic structure methods. Dispersion-corrected DFT results are labelled as '+d3'. Experimentally measured interaction energy for neutral Ar-Ar case is shown as horizontal dashed lines. Energy is in E_h and interatomic distance is in Å.

corrections included is very close to the Aziz data. However, it significantly overestimates the binding energy for the Ar-Ar$^+$ dimer as indicated by the discrepancy with respect to the coupled cluster curve.

For the current DFTB simulations we used the MIO parameter set to describe C-C and C-H interactions [77]. The CCSD(T) theory, which intrinsically includes dispersion interaction, along with 6-311++G(3df,3pd) basis, was used for the repulsion term (E_{rep}) of DFTB with a 1.6 nm cutoff [78, 79]. The Slater-Koster parameters (Hamiltonian and overlap matrices) for Ar-Ar, Ar-C and Ar-H were prepared from higher level, all-electron DFT with long-range corrected (LC)-wPBEh functional calculations and a 6-311++G(3df,3pd) basis set. The new Ar parameter set included s and p valence orbitals.

The DFTB simulations of graphene irradiation with an Ar_n^+ beam were performed within the Born-Oppenheimer approximation and with Fermi-Dirac smearing (T_{el}=1000 K). The electronic temperature and Fermi-Dirac smearing effectively improves SCF convergence for processes in which a significant number of bonds are being broken and/or formed. The time step for molecular dynamics was set to 0.5 fs. The initial energy of the Ar_n^+ beam in the simulations was varied from 2.5 eV to 25 eV per Ar atom. This corresponds to a total beam energy ranging from 2.5 keV to 25 keV.

The representative snapshots from direct dynamics of graphene irradiation with Ar_n^+ using DFTB are shown in Figure 3. The supported and suspended graphene layers show different behavior under Ar_n^+ beam irradiation. The irradiation of the suspended graphene induced vacancies and nanopores, with a threshold of ∼15 eV per Ar atom for rupturing of the suspended graphene. However, no significant damage to supported graphene was observed with even higher beam energies. The mechanism for the Ar_n^+ induced damage of the suspended graphene involves significant deformation of

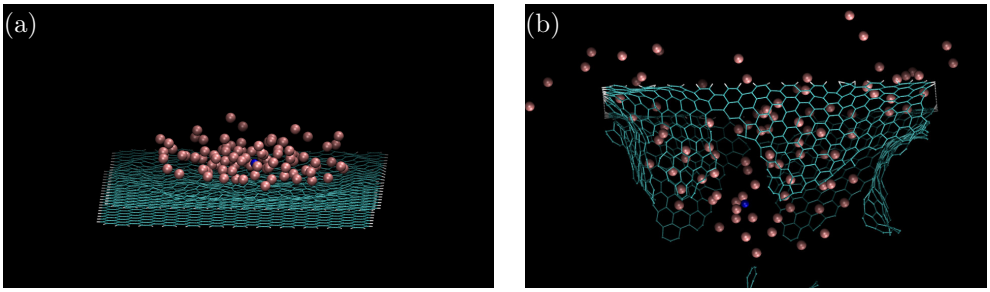

Figure 3: Ab initio MD simulations using DFTB of (a) a supported graphene irradiated with an Ar^+_{100} cluster of 2.5 keV beam energy (25 eV per Ar atom) captured at 0.55 ps showing no surface damage and of (b) a suspended graphene irradiated with an Ar^+_{100} cluster of 1.5 keV beam energy (15 eV per Ar atom) captured at 1.0 ps showing rupturing of graphene. The Ar^+ that carries the charge is shown in blue.

the graphene layer prior to its rupture, which is initiated by C-C bond breaking after the impact of the Ar^+_n beam. For supported graphene, this would require a much higher beam energy. Effectively the support underneath graphene membrane facilitates the redistribution and dissipation of kinetic energy deposited by Ar^+_n beam during the impact as indicated by the outgoing concentric wave propagating away from impact point as visible in Figure 3(a).

3.2 Graphene irradiation with an energetic H beam

Next we discuss the results of classical molecular dynamics of graphene bombarded by a H beam for impact energies up to 200 eV. Generally speaking, hydrogen beams can be provided in the form of both H_2 molecules and H atoms [80, 81], the latter of which is for our concern in this chapter. In this energy regime the incident hydrogen behaves classically and NQE can be neglected. Understanding the effect of interaction of energetic hydrogen with graphene is important for understanding of the damage of plasma facing carbon tile in the ITER fusion reactor [6, 82, 83]. Also, graphene-based electronic systems in space vehicles might be sensitive to the damage caused by cosmic radiation containing a wide spectrum of particles, a significant component of which would be light atoms from solar wind [6]. The defects caused by energetic light particles include lattice defects, creation of vacancies, as well as chemical changes.

To simulate effects of irradiation on graphene one can apply direct molecular dynamics methods in which electronic structure is treated explicitly using quantum mechanics, while the motion of the nuclei is described using classical molecular dynamics. This allows to accurately describe bond breaking and formation due to the interaction of graphene with projectile hydrogen and related chemical changes. Such an approach is however limited by the computational cost of electronic structure theory. Employing DFTB instead of DFT allows alleviating this limitation in the system

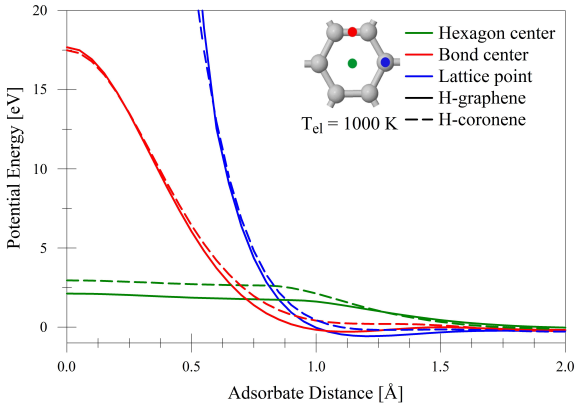

Figure 4: Potential energies of the hydrogen-coronene and hydrogen-graphene interaction calculated with DFTB method as a function of distance for different impact positions. Reprinted with permission from Ref. [6].

sizes, time scales, and statistics that can be obtained.

Here, the initial structure of 3×3 nm^2 graphene sheet with 336 C atoms was obtained from Nose-Hoover thermostated DFTB molecular dynamics at 300 K. To include the effect of statistical uncertainty in the irradiation, for each impact energy 1000 independent trajectory simulations were performed with randomly chosen initial positions of the incident H atom above the surface of the graphene sheet. We note that the usual DFTB parameters are not suitable to describe short range interatomic interactions as those distances are not relevant for the expected chemistry. To allow for the high-energy impact, the repulsive part of DFTB parameters (PBC-0-3 set) was fitted to the binary Ziegler-Biersack-Littmark repulsive potentials [84, 85].

Figure 4 compares the DFTB potential energies of hydrogen-graphene and hydrogen-coronene as a function of H position above the graphene/coronene plane. The coronene potentials show bonding that is roughly 1 eV weaker and a potential barrier at the hexagon center that is 1 eV higher, reflecting the changes in electronic structure between hydrogen-terminated and periodic sp^2 carbon. Despite these differences, the forms of the H-graphene and H-coronene interactions are very similar, highlighting that short range potentials are critical for high energy impact. Furthermore, the DFTB results for the H-coronene system agree qualitatively well with the DFT calculations in Ref. [86]. These observations combined together suggest that the DFTB parameters are acceptable alternative of more expensive DFT potentials for the study of graphene.

The DFTB simulations of irradiation show three possible outcomes: adsorption, reflection, and transmission of incident hydrogen, without observing sputtering. The adsorption is observed for incident energies not exceeding 1 eV, as shown in the left panel in Figure 5. The reflection of H dominates in a mid-energy range between 1 and 10 eV with the probability peak at approximately

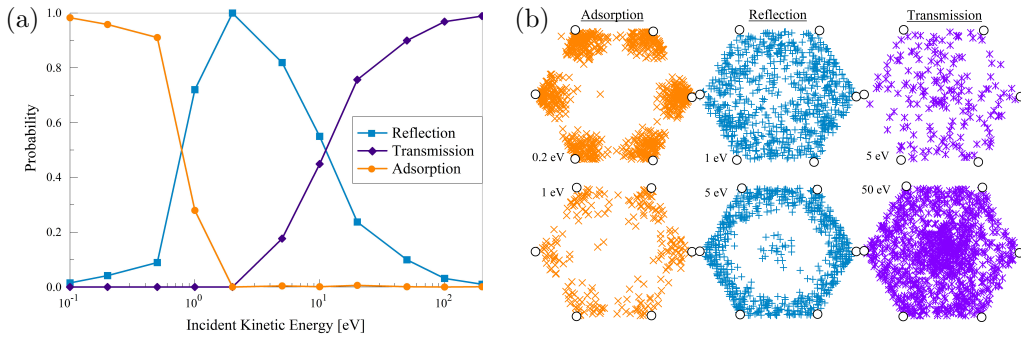

Figure 5: (a) Adsorption, reflection, and transmission probabilities for H irradiation of graphene as a function of incident energy. (b) Positions of adsorption, reflection, and transmission events for the quantum-classical calculations for selected incident energies. Position of carbon atoms are shown as white circles. Reprinted with permission from Ref. [6].

2 eV. The threshold for transmission of H through graphene should be greater than 2 eV. Indeed, the energy barrier for H transfer across graphene is about 3-4 eV from DFT calculations [87, 88]. For high energies up to 200 eV, the event is mainly transmission with insignificant reflection.

By examining the position within the hexagon where incident hydrogens are adsorbed, reflected, or transmitted (see right panel in Figure 5), one can infer the nature of the interaction potential. Maximum adsorption clearly indicates the position of lattice atoms. Probability clustering around the carbon atoms also shows their in-plane lattice vibrations. Reflection can occur at every position in the graphene hexagon (see 1 eV), but the clustering for incident energies of 5 eV indicates a CC bonding network. The transmission of H is most probable near the center of hexagons.

3.3 Classical vs quantum simulations of H and D adsorption on graphene

Next we turn to the modeling of H/D adsorption on graphene in the low energy regime. As shown above, during graphene irradiation with atomic hydrogen, reflection and transmission are the prevalent processes at high kinetic energy of the incident atoms, while the regime of low incident energies (below 1 eV) is dominated by the hydrogen adsorption. During low-energy motion of hydrogen, the NQEs such as the zero-point energy (ZPE) and tunneling become more prominent and may influence chemical reactivity [10, 11, 89, 90]. Therefore, it is essential to account for the quantum mechanical nature of low-energy hydrogen, and to accurately reproduce the potential energy landscape, in particular the energy barriers. To be able to describe this regime, we have tuned the DFTB potential using electronic temperature as as tuning parameter so that the features of the PES important for adsorption of H and D on graphene are reasonably well-reproduced as shown in Figure 6. See Ref. [56] for details on the procedure used to adjust the DFTB parameters.

We use the approximate quantum trajectory dynamics, summarized in Section 2.3, based on

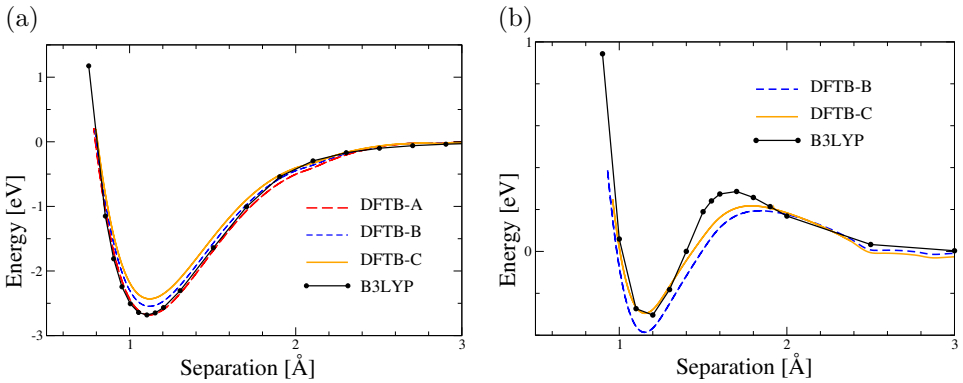

Figure 6: Comparison of the DFTB and DFT/B3LYP energy for interaction of H with a graphene flake $C_{37}H_{15}$ along the normal to the graphene surface above C atom (lattice center) as a function of separation between H and C. (a) The structure of a graphene flake is allowed to fully relax as the incident H approaches the C center of the graphene surface (slow motion limit). (b) The structure of graphene is completely frozen during the potential energy scan (fast motion of H limit). For DFTB the potential energy was adjusted using electronic temperature as a parameter. The labels A,B,C correspond to different values of the tuning parameter. Adapted with permission from Ref. [56]; copyright 2014 American Chemical Society.

the evolution of an ensemble of interdependent trajectories to describe the quantum nature of incident "light" hydrogen, combined with classical newtonian dynamics of remaining "heavy" atoms, and with the DFTB description of electronic structure. The quantum-mechanical effects are introduced via the quantum potential, determined by the time-evolution of the nuclear wavefunction. The corresponding quantum force, added to the usual classical force determined by the electronic structure of a system, formally generates all NQEs within the trajectory description of the wavefunction dynamics. The linearized quantum force used here – derived from the simplest globally defined approximation to the quantum potential – is exact for a Gaussian-type wavefunctions, and it captures the leading NQEs, e.g. the ZPE, energy of wavefunction localization, moderate tunneling and wavefunction bifurcation [41].

As noted in the previous section, the most reactive condition for hydrogen adsorption is when the incoming hydrogen collides with the lattice center (carbon atom) as opposed to the center of the CC bond or with the hexagon center, especially at low incident energy. In general, the carbon bonding network dynamically responds to the impact of incident hydrogen. The carbon lattice can absorb some fraction of the kinetic energy of incident hydrogen in the course of dynamics and change hybridization from sp^2 to sp^3 depending on the kinetic energy of hydrogen.

Overall, the potential experienced by incoming hydrogen will fall between two limiting cases: (a) vibrationally 'adiabatic' collision in which the carbon bonding network can fully relax and hybridization can change from sp^2 to sp^3 in response to incoming atom, and (b) vibrationally 'diabatic'

collision with a frozen carbon network, when the collision time is too short for the carbon network to adapt to the approaching hydrogen atom. The corresponding potential energy surfaces (PES) for a graphene flake $C_{37}H_{15}$ calculated from three sets of adjusted DFTB parameters and DFT are plotted in Figure 6. In the case of the adiabatic process, which is the typical evolution of a system along the 'reaction path', the relaxation of the carbon bonding network in graphene results in the rehybridization of the C atom from sp^2 to sp^3, leading to the barrierless formation of a covalent CH bond sitting in a deep potential well of ∼2.5 eV. In contrast, the PES describing the diabatic process, i.e. the positions of the carbon atoms do not change during the collision process, reveals that the incoming H experiences a low energy barrier on the level of 0.2 eV followed by a shallow well on the level of only 0.4 eV. The actual potential experienced by incoming hydrogen depends on its kinetic energy and falls in between these two limiting situations.

The dynamics simulations show that hydrogen adsorption occurs in four consecutive steps: (1) hydrogen passes over the barrier, (2) inelastic collision of hydrogen with the planar sp^2 graphene, which leads to the transfer of a portion of its kinetic energy to graphene, (3) a physisorption stage in which the H atom becomes trapped in the shallow well of potential energy after partial deposition of its kinetic energy with C in a sp^2 configuration, and (4) conversion of physisorption into chemisorption through the relaxation of the graphene lattice and formation of a CH bond with C in the sp^3 configuration. The last step of graphene lattice relaxation is the slowest one. Several vibrational C-H oscillation cycles were observed in MD simulations before graphene lattice reorganized and corresponding force constants (and frequencies) for C-H vibrations changed from the value corresponding to sp^2 hybridization to sp^3 ones [56].

We now discuss NQE and the effects of the quantum corrections on the dynamics of H observed with the ensemble of quantum trajectory dynamics and on the evolution of the graphene flake (classical part of the system). First, turning off the quantum potential within the quantum trajectory simulations turns the ensemble of quantum trajectories into an ensemble of classical trajectories. This allows to directly estimate the effects of neglecting quantum correlations between trajectories by turning *on* and *off* the quantum potential. Next, the (quasi)classical part of the system, that is the carbon network lattice, experiences a force from the quantum part of a system that is averaged over the ensemble of trajectories. The results in Figure 7(a) are obtained using the Ehrenfest-type treatment, where first we calculate an ensemble averaged expectation value for the hydrogen position and then use this position to calculate forces acting on graphene. The results of (quasi)classical-like [29] description of graphene are presented in Figure 7(b).

The simulations with the classical treatment of H, i.e., with quantum potential turned off, show sharp change in adsorption probability that corresponds to a well defined energy window for adsorp-

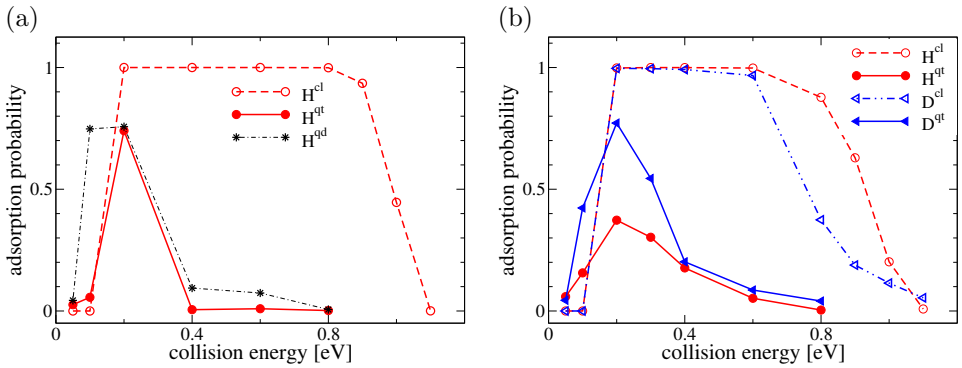

Figure 7: Probabilities for adsorption of H and D atoms on graphene as a function of the collision energy. Superscripts 'qt' and 'cl' refer to the probabilities from the dynamics with and without the quantum correction on the force. Dynamics with the graphene atoms initially at equilibrium (single QT ensemble) and with the ZPE distribution (multiple QT ensembles) are shown in panels (a) and (b), respectively. Results of the reduced-dimensionality exact quantum dynamics of H in a time-dependent potential (panel (a), details in text) are labeled 'qd'. Adapted with permission from [37]; copyright 2013 American Chemical Society.

tion. This can be understood intuitively in the following way. For the very small incident energies that are below the adsorption window, all trajectories are reflected from the barrier energy. For the incident energies falling within the adsorption window the incident hydrogen has enough kinetic energy to pass above the barrier and to collide with the repulsive wall at short range. The collision leads to H transferring some of its kinetic energy to graphene network and becoming trapped in the potential well between the short range repulsive wall and the barrier. Finally, for the kinetic energies above the adsorption window, the incident H passes above the barrier and transfers some of its energy to the graphene flake, but the change in its kinetic energy is too small for H to become trapped in the potential well, resulting instead in reflection.

The main NQE observed in this system is that the quantum potential, i.e. the localization energy of the initial wavefunction, effectively spreads the momenta of individual quantum trajectories as they exchange energy, whereas in the classical case all trajectories start out with the same momenta and do not exchange energy. Thus, their adsorption probability is nearly 'binary' resulting in the adsorption 'window' of $[0.2, 1.0]$ eV. In the QT simulation, even for the collision energies below 0.2 eV, the QTs at the leading edge of the wavepacket gets the energy boost from the QT ensemble, thus certain fraction of the QTs has sufficient energy to cross the barrier and become adsorbed at the lattice center. This behavior can be viewed as shallow to moderate tunneling, when compared to the exact quantum simulation on a grid performed in one-dimension along the collision coordinate, using the time-dependent potential from the QT simulation. In the exact quantum dynamics simulation, the adsorption probability at 0.1 eV is higher than for the QT dynamics, while the classical dynamics

at this energy gives zero adsorption.

At higher collision energies, we attribute the reduced adsorption probability in the QT simulation to a significant fraction of trajectories being too 'energetic' for effective energy exchange with the graphene, something that happens in the classical simulation at energies above 1 eV. We do note, however, that the classical and QT dynamics unfolds on effectively different potential energy surfaces since the classical force acting on the carbon atoms is averaged over the ensembles of trajectories, which have different positions with and without the quantum correction on dynamics.

To relax the Ehrenfest treatment of the graphene flake, we have also introduced sampling of the carbon positions according to the ZPE of the C-C stretch. The adsorption probability, averaged over multiple QTs ensembles, is shown in Figure 7. These ensembles are independent of each other; and we find that 11 and 14 ensembles were adequate for the average probabilities computed for H and D, respectively. The overall trend in probabilities obtained from the dynamics with and without the quantum correction is similar to that discussed above. Comparing the isotopes, both H and D show a well-defined adsorption peak at 0.4 eV; the higher adsorption probability for D is explained by the relatively longer interaction times of D (which for the same kinetic energy moves slower than H) with the graphene flake, allowing for more efficient transfer of the collision energy to the graphene flake. At the collision energy of 0.2 eV, the ratio of adsorption probabilities is close to 3, which is not observed in the classical simulations, an effect that could be tested experimentally. Finally we note that the difference between the classical and QT simulations involving D is reduced compared to that for H, an expected dependence on the mass of quantum particles.

3.4 Transmission of H^+ and D^+ through graphene and hBN

Finally we discuss the transmission of protons and deuterons (H^+ and D^+) through graphene and its isoelectronic analogue hBN. Understanding transmission of small molecules and species through graphene and other atomically thin two-dimensional materials is of great importance for potential applications as membranes suitable for sieving gases, liquids, and separation of hydrogen isotopes. Here we focus on the role of NQEs and isotopic substitution effects on the transmission rates [91]. As discussed above, when the kinetic energy of neutral H is on the level of 1 eV or less, the only observed processes are adsorption and reflection of H. Transmission of H through graphene can be observed when its kinetic energy is on the level of a couple of eV, especially for collision through the hexagon center. However, the situation is very different for transmission of charged species in a liquid environment.

It has been experimentally demonstrated that mono-layer of graphene and mono- and bi-layer of hBN are permeable to H^+ at room temperature, but are not permeable to H [71]. The experimental

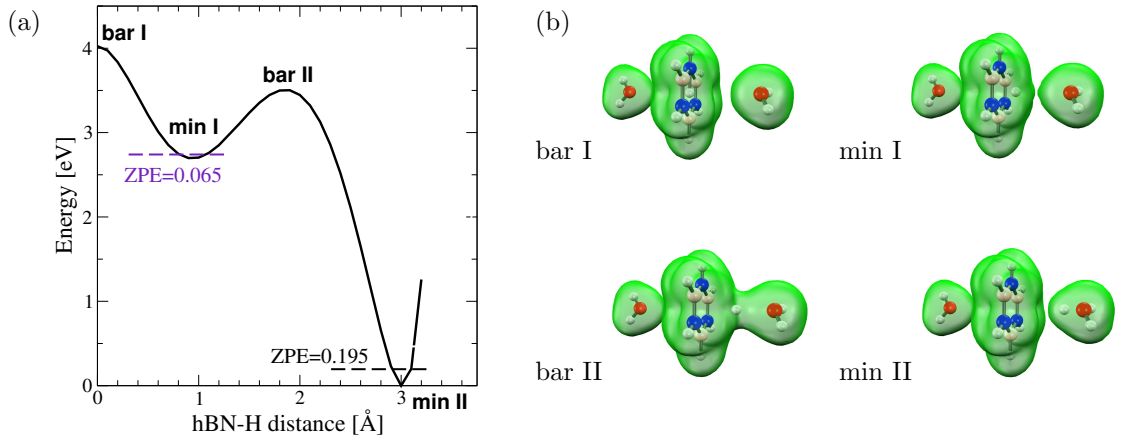

Figure 8: (a) The potential energy profile for the proton transmission through borazine ($B_3H_3N_3$) computed at the CCSD/6-31G** level shown as a function of r. The ZPE-corrected energies at the minima are indicated with dashes. Only the ZPE along the proton transfer coordinate is considered. Hydrogen bonding with environmental water is characterized by two barriers, labeled as 'bar I' at $r = 0$ Å and 'bar II' at $r = 2$ Å, and two minima labeled as 'min I' at $r = 1$ Å and 'min II' at $r = 3$ Å, where r is the proton-ring distance. (b) The respective electronic densities, computed at the MP2/cc-PVTZ level, are shown for the oxygen-ring distance fixed at $R = 4.0$ Å. Reprinted with permission from [91]; copyright 2017 American Chemical Society.

device consisted of graphene and hBN membranes immersed in Nafion, which is a proton conducting polymer [92]. The dependence of proton conductivity as a function of temperature was measured. The results were fit with an Arrhenius expression $\exp(-E_a/k_BT)$ from which activation energies, E_a, for proton transmission were estimated to be 0.3 eV for hBN and 0.78 eV for graphene. These activation energies are systematically lower than the theoretical barriers in the ranges of [0.7, 1.0] eV and [1.2, 1.5] eV for mono-layer hBN and graphene, respectively [71, 87, 91, 93, 94, 95, 96, 97, 98]. It has also been shown that the transmission of a proton is 10 times greater than that of a deuteron, with the difference attributed to the zero-point energy [99].

The proton and deuteron transfer in the experimental setting involves a network of hydrogen bondings. The simplest model that accounts for energetic effects of hydrogen bonding relies on two water molecules flanking the two sides of the membrane to serve as proton donor and acceptor. In such case the overall process can be written as:

$$H_3O^+ - M - H_2O \longrightarrow H_2O - M - H_3O^+ \tag{21}$$

where M is a graphene or hBN membrane. The resulting potential energy profile for proton transmission through the membrane is characterized by two energy minima and two barriers. Figure 8 shows the potential energy for hydrogen transmission through borazine ($B_3H_3N_3$), the smallest model for hBN, as a function of distance from the membrane's surface and corresponding molecular structures.

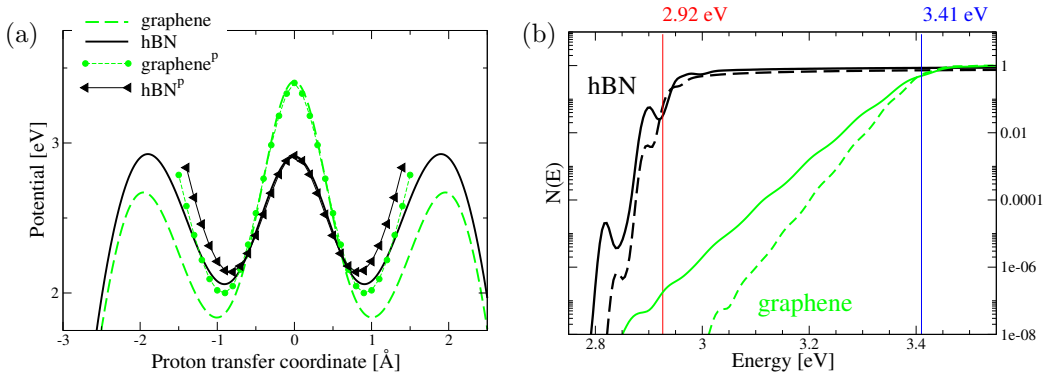

Figure 9: (a) The potential energy profile as a function of the proton-membrane separation. The membrane is modeled with 19 rings with two water molecules (proton donor and acceptor) on both sides of the membrane. Similar gas phase curves (without the water molecules) are shown for comparison and labelled with 'p' superscript. (b) The energy-dependent transmission probabilities for hBN (black) and graphene (green) interacting with the proton (solid line) and deuteron (dashed line). The barrier heights are marked with vertical lines (red) for hBN at 2.92 eV and (blue) for graphene at 3.41 eV. Reprinted with permission from [91]; copyright 2017 American Chemical Society.

The potential energy on the other side of the membrane is simply a mirror image. At the minimum I proton is adsorbed at the surface of the membrane (borazine's hexagon here) whereas at minimum II the proton is involved in hydrogen bonding with nearby water forming hydronium. To remove a proton from hydronium, external work is required to break the hydrogen bond in hydronium which is represented by barrier II. Similarly passing through the center of a hexagon ring of the membrane requires work (barrier I) to 'loosen' the bonding network in the membrane to open a transmission channel.

Here we describe the simulation of proton and deuteron transfer through graphene and hBN membranes. In both cases the models of the membrane are constructed as optimized graphene and hBN flakes consisting of 19 fused hexagonal rings [91]. The potential energy surfaces for graphene and hBN are obtained from coupled cluster theory and are shown on Figure 9(a). As can be seen, the barrier I for the graphene flake is 0.5 eV higher than for hBN. This is consistent with higher permeability and lower activation energy for a hBN membrane than for a graphene membrane. The membrane itself was frozen during simulations. The simulation of proton and deuteron transmission was achieved by employing an exact one dimensional quantum dynamics model along the normal direction to the membrane surface. The quantum dynamical model was based on wavepacket correlation-function formulation of S-matrix scattering theory [100]. The reactant and product states correspond to H_3O^+ or H_2DO^+ on different sides of membrane and are described by Gaussian wavepacket localized at minimum II. Noticeably, transmission of proton or deuteron through a membrane requires passing through three energy barriers: twice through barrier II (on both sides

of membrane) and once through barrier I (at the center of membrane). The proton and deuteron transmission probabilities $N(E)$ for a graphene and hBN membrane as a function of kinetic energy, E, are shown on Figure 9(b). Simulations show that the proton is more likely to transfer through the membrane than the deuteron. The resonant maxima of transmission probabilities for hBN are attributed to its triple barrier. That is, the non-monotonic transmission probabilities are due to shallow tunneling and above-barrier reflection when the wavepacket energy is comparable with the barrier height. Contrary to this the transmission through graphene is determined by a single barrier I which dominates the entire energy profile. Overall, more classical transmission and smaller proton/deuteron isotope effects for hBN are expected than for graphene after thermal averaging.

Next, from the energy dependent transmission probabilities, $N(E)$, the quantum thermal rate constants $k(T)$ are obtained as an average over Boltzmann factor $k^q(T) = (2\pi Q(T))^{-1} \int_0^\infty N(E) \cdot \exp(-E/k_B T) dE$, where $Q(T)$ is the translational partition function. Similarly, classical thermal rates are related to the barrier height V_b as $k^{cl}(T) = k_B T/(2\pi Q(T)) \exp(-V_b/k_B T)$, which is directly related to experimentally measured activation energy E_a through the Arrhenius reaction rate expression $k^A(T) = A \exp(-E_a/k_B T)$. Finally, the tunneling factor $\kappa(T) = k^q(T)/k^{cl}(T)$ is obtained from the ratio of quantum and classical rate constants. Our estimates for the room temperature kinetic isotope effect (KIE) are 3-4 for hBN and 20-30 for graphene, whereas the experimental values are closer to 10 for both systems. We note that 1D models tend to exaggerate quantum effects while full ab initio dynamics involving dynamical membrane relaxation along with a more realistic 3D quantum treatment of protons such as quantum trajectories is expected to give results closer to experiment. Nevertheless, 1D quantum models for quantum treatment of selected protons provide an inexpensive first approximation for estimation of NQEs and isotopic substitution effects.

Summary

There are significant experimental and theoretical interests in application of beams of atomic and ionic clusters and species for graphene engineering. In this chapter, we have presented techniques for direct dynamics modeling of irradiation of graphene with beams of atomic and ionic species. The discussed techniques include both classical and quantum trajectory methods in conjunction with DFTB. Nuclear quantum effects and isotopic substitution effects are also discussed. Depending on the type of particles in the beam and the beam energy, the irradiation can lead to different physical effects. The specific choice of methodology and its validity for description of graphene irradiation depend on the mass and energy of beam particles. All simulations presented here assume that electronic excitations can be neglected during the nuclear motion and that the ground electronic state sufficiently describes the potential energy during the dynamics. This is not always the case.

In the next chapter (Chapter 8), we discuss the effect of electronic excitation in the beam-matter interactions.

Acknowledgments

This work was conducted at the Center for Nanophase Materials Sciences of the Oak Ridge National Laboratory, a U.S. Department of Energy Office of Science User Facility. This work used the Extreme Science and Engineering Discovery Environment (XSEDE), which is supported by National Science Foundation grant No. ACI-1548562 (allocation TG-DMR110037) and resources of the Oak Ridge Leadership Computing Facility (OLCF) and of the Compute and Data Environment for Science (CADES) at the Oak Ridge National Laboratory, which is supported by the Office of Science of the U.S. Department of Energy under Contract No. DE-AC05-00OR22725. SG acknowledges partial support by the National Science Foundation under Grants CHE-1955768 and CHE-1565985. Any Opinions, findings and conclusions or recommendations expressed in this material are those of the authors and do not necessarily reflect those of the National Science Foundation.

References

[1] Vasilios Georgakilas, Michal Otyepka, Athanasios B. Bourlinos, Vimlesh Chandra, Namdong Kim, K. Christian Kemp, Pavel Hobza, Radek Zboril, and Kwang S. Kim. Functionalization of graphene: Covalent and non-covalent approaches, derivatives and applications. *Chemical Reviews*, 112:6156–6214, 2012.

[2] Young-Woo Son, Marvin L. Cohen, and Steven G. Louie. Energy gaps in graphene nanoribbons. *Pysical Review Letters*, 97:216803, 2006.

[3] Veronica Barone, Oded Hod, and Gustavo E. Scuseria. Electronic structure and stability of semiconducting graphene nanoribbons. *Nano Letters*, 6:2748–2754, 2006.

[4] Veronica Barone and Juan E. Peralta. Magnetic boron nitride nanoribbons with tunable electronic properties. *Nano Letters*, 8:2210–2214, 2008.

[5] Alejandro Lopez-Bezanilla, Jingsong Huang, Humberto Terrones, and Bobby G. Sumpter. Boron nitride nanoribbons become metallic. *Nano Letters*, 11:3267–3273, 2011.

[6] Robert C. Ehemann, Jonny Dadras, Paul R. C. Kent, Jacek Jakowski, and Predrag S. Krstic. Detection of hydrogen using graphene. *Nano Research Letters*, 7:198, 2012.

[7] I. Deretzis, G. Fiori, G. Iannaccone, G. Piccitto, and A. La Magna. Quantum transport modeling of defected graphene nanoribbons. *Physica E*, 44:981–984, 2012.

[8] N. Gorjizadeh and Y. Kawazoe. Chemical functionalization of graphene nanoribbons. *Journal of Nanomaterials*, 20:1–7, 2010.

[9] K. Wakabayashi, Y. Takane, M. Yamamoto, and M. Sigrist. Electronic transport properties of graphene nanoribbons. *New Journal of Physics*, 11:095016, 2009.

[10] M. Karplus, R. N. Porter, and R. D. Sharma. Exchange reactions with activation energy. I. Simple barrier potential for (H, H_2). *Journal of Chemical Physics*, 43:3259–3287, 1965.

[11] X. Zhu, P. Lopes, and A. D. MacKerell. Recent developments and applications of the CHARMM force fields. *Wiley Interdisciplinary Reviews – Computational Molecular Science*, 2:167–185, 2012.

[12] J. C. Light and T. Carrington Jr. Discrete variable representations and their utilization. *Advances in Chemical Physics*, 114:263–310, 2000.

[13] F. Huarte-Larranaga and U. Manthe. Quantum dynamics of the $CH_4 + H \rightarrow CH_3 + H_2$ reaction: Full-dimensional and reduced dimensionality rate constant calculations. *Journal of Physical Chemistry A*, 105:2522–2529, 2001.

[14] D. V. Shalashilin and I. Burghardt. Gaussian-based techniques for quantum propagation from the time-dependent variational principle: Formulation in terms of trajectories of coupled classical and quantum variable. *Journal of Chemical Physics*, 129:084104, 2008.

[15] H. D. Meyer, U. Manthe, and L. S. Cederbaum. The multi-configurational time-dependent hartree approach. *Chemical Physics Letters*, 165:73–78, 1990.

[16] H. B. Wang and M. Thoss. Multilayer formulation of the multiconfiguration time-dependent hartree theory. *Journal of Chemical Physics*, 119:1289–1299, 2003.

[17] I. Burghardt, H.-D. Meyer, and L. S. Cederbaum. Approaches to the approximate treatment of complex molecular systems by the multiconfiguration time-dependent hartree method. *Journal of Chemical Physics*, 111:2927–2939, 1999.

[18] M. Ben-Nun, J. Quenneville, and T. J. Martinez. *Ab initio* multiple spawning: Photochemistry from first principles quantum molecular dynamics. *Journal of Chemical Physics*, 104:5161–5175, 2001.

[19] D. V. Shalashilin and M. S. Child. Time dependent quantum propagation in phase space. *Journal of Chemical Physics*, 113:10028–10036, 2000.

[20] R. Martinazzo, M. Nest, P. Saalfrank, and G. F. Tantardini. A local coherent-state approximation to system-bath quantum dynamics. *Journal of Chemical Physics*, 125:194102, 2006.

[21] Y. H. Wu and V. S. Batista. Matching-pursuit for simulations of quantum processes. *Journal of Chemical Physics*, 118:6720–6724, 2003.

[22] S. Y. Kim and S. Hammes-Schiffer. Hybrid quantum/classical molecular dynamics for a proton transfer reaction coupled to a dissipative bath. *Journal of Chemical Physics*, 124:244102, 2006.

[23] O. Prezhdo and V. V. Kisil. Mixing quantum and classical mechanics. *Physical Review A*, 56:162–175, 1997.

[24] J. Gao and D. G. Truhlar. Quantum mechanical methods for enzyme kinetics. *Annual Review of Physical Chemistry*, 53:467–505, 2002.

[25] Gabor Naray-Szabo and Arieh Warshel. *Computational approaches to biochemical reactivity*, volume 19. Kluwer Academic Publishers, New York, NY, 1997.

[26] O. V. Prezhdo and C. Brooksby. Quantum backreaction through the bohmian particle. *Physical Review Letters*, 86:3215–3219, 2001.

[27] S. S. Iyengar and J. Jakowski. Quantum wave packet *Ab Initio* molecualr dynamics. *Journal of Chemical Physics*, 122:114105, 2005.

[28] W. H. Miller. The semiclassical initial value representation: A potentially practical way for adding quantum effects to classical molecular dynamics simulations. *Journal of Physical Chemistry A*, 105:2942–2955, 2001.

[29] G. C. Schatz, J. M. Bowman, and A. Kuppermann. Exact quantum, quasiclassical, and semiclassical reaction probabilities for collinear F + D_2 $\rightarrow$ FD + D reaction. *Journal of Chemical Physics*, 63:685–696, 1975.

[30] F. Paesani and G. A. Voth. The properties of water: Insights from quantum simulations. *Journal of Physical Chemistry B*, 113:5702–5719, 2009.

[31] S. Habershon and D. E. Manolopoulos. Zero point energy leakage in condensed phase dynamics: An assessment of quantum simulation methods for liquid water. *Journal of Chemical Physics*, 131:244302, 2009.

[32] D. Marx, M. E. Tuckerman, and G. J. Martyna. Quantum dynamics via adiabatic *ab initio* centroid molecular dynamics. *Computer Physics Communications*, 118:166–184, 1999.

[33] J. Jakowski and K. Morokuma. Liouville-von Neumann molecular dynamics. *Journal of Chemical Physics*, 130:224106, 2009.

[34] O. V. Prezhdo and P. J. Rossky. Mean-field molecular dynamics with surface hopping. *Journal of Chemical Physics*, 107:825, 1997.

[35] Heather M. Jaeger, Sean Fischer, and Oleg V. Prezhdo. Decoherence-induced surface hopping. *Journal of Chemical Physics*, 137:22A545, 2012.

[36] Michael J. Bedard-Hearn, Ross E. Larsen, and Benjamin J. Schwartz. Mean-field dynamics with stochastic decoherence MF-SD: A new algorithm for nonadiabatic mixed quantum/classical molecular-dynamics simulations with nuclear-induced decoherence. *Journal of Chemical Physics*, 123:234106, 2005.

[37] Sophya Garashchuk, Jacek Jakowski, Lei Wang, and Bobby G. Sumpter. Quantum trajectory-electronic structure approach for exploring nuclear effects in the dynamics of nanomaterials. *Journal of Chemical Theory and Computation*, 9:5221–5235, 2013.

[38] P. Ehrenfest. Bemerkung über die angenäherte Gültigkeit der klassischen Mechanik innerhalb der Quantenmechanik. *Zeitschrift für Physik*, 45:455–457, 1927.

[39] D. Bohm. A suggested interpretation of the quantum theory in terms of "hidden" variables, I and II. *Physical Review*, 85:166–193, 1952.

[40] V. A. Rassolov, S. Garashchuk, and G. C. Schatz. Quantum trajectory dynamics in arbitrary coordinates. *Journal of Physical Chemistry A*, 110:5530–5536, 2006.

[41] S. Garashchuk and V. A. Rassolov. Energy conserving approximations to the quantum potential: Dynamics with linearized quantum force. *Journal of Chemical Physics*, 120:1181–1190, 2004.

[42] Sophya Garashchuk, Vitaly Rassolov, and Oleg Prezhdo. *Reviews in Computational Chemistry*, volume 27, chapter Semiclassical Bohmian dynamics, pages 111–210. Wiley, 2011.

[43] V. A. Rassolov and S. Garashchuk. Computational complexity in quantum chemistry. *Chemical Physics Letters*, 464:262–264, 2008.

[44] W. H. Press, B. P. Flannery, S. A. Teukolsky, and W. T. Vetterling. *Numerical Recipes: The Art of Scientific Computing*. Cambridge University Press, Cambridge, 3 edition, 2007.

[45] V. A. Rassolov and S. Garashchuk. Bohmian dynamics on subspaces using linearized quantum force. *Journal of Chemical Physics*, 120:6815–6825, 2004.

[46] S. Garashchuk and M. V. Volkov. Incorporation of quantum effects for selected degrees of freedom into the trajectory-based dynamics using spatial domains. *Journal of Chemical Physics*, 137:074115, 2012.

[47] Sophya Garashchuk and Vitaly Rassolov. Quantum trajectory dynamics based on local approximations to the quantum potential and force. *Journal of Chemical Theory and Computation*, 15:3906–3916, 2019.

[48] Bing Gu, Robert J. Hinde, Vitaly A. Rassolov, and Sophya Garashchuk. Estimation of the ground state energy of an atomic solid by employing quantum trajectory dynamics with friction. *Journal of Chemical Theory and Computation*, 11:2891–2899, 2015.

[49] S. Godecker. Linear scaling electronic structure methods. *Reviews of Modern Physics*, 71:1085, 1999.

[50] Christoph Bannwarth, Sebastian Ehlert, and Stefan Grimme. GFN2-xTB—An accurate and broadly parametrized self-consistent tight-binding quantum chemical method with multipole electrostatics and density-dependent dispersion contributions. *Journal of Chemical Theory and Computation*, 15:1652–1671, 2019.

[51] G. Zheng, M. Lundberg, J. Jakowski, T. Vreven, M. Frisch, and K. Morokuma. Implementation and benchmark tests of the dftb method and its application in the oniom method. *International Journal of Quantum Chemistry*, 109:1841–1854, 2009.

[52] M. Elstner, D. Porezag, G. Jungnickel, J. Elsner, M. Haugk, Th. Frauenheim, S. Suhai, and G. Seifert. Self-consistent-charge density-functional tight-binding method for simulations of complex materials properties. *Physical Review B*, 58:7260–7268, 1998.

[53] D. Porezag, T. Fraunheim, T. Kohler, G. Seifert, and R. Kaschner. Construction of tight-binding-like potentials on the basis of density-functional theory: Application to carbon. *Physical Review B*, 51:12947–12957, 1995.

[54] J. Mazzuca, S. Garashchuk, and J. Jakowski. Description of proton transfer in soybean lipoxygenase-1 employing approximate quantum trajectory dynamics. *Chemical Physics Letters*, 542:153–158, 2012.

[55] Jacek Jakowski, B. Hadri, S. J. Stuart, P. Krstic, S. Irle, D. Nugawela, and S. Garashchuk. Optimization of density functional tight-binding and classical reactive molecular dynamics for high-throughput simulations of carbon materials. *XSEDE'12, Conference Proceedings. ACM.*, 36:1–7, 2012.

[56] Lei Wang, Jacek Jakowski, and Sophya Garashchuk. Adsorption of a Hydrogen Atom on a Graphene Flake Examined with Quantum Trajectory/Electronic Structure Dynamics. *Journal of Physical Chemistry C*, 118:16175–16187, 2014.

[57] D. C. Bell, M. C. Lemme, L. A. Stern, J. R. Williams, and C. M. Marcus. Precision cutting and patterning of graphene with helium ions. *Nanotechnology*, 20:455301, 2009.

[58] A. Dey, A. Chroneos, N. S. Braithwaite, R. P. Gandhiraman, and S. Krishnamurth. Plasma engineering of graphene. *Applied Physical Reviews*, 3:021301, 2016.

[59] Vighter Iberi, Ivan Vlassiouk, X.-G. Zhang, Brad Matola, Allison Linn, David C. Joy, and Adam J. Rondinone. Maskless lithography and in situ visualization of conductivity of graphene using helium ion microscopy. *Scientific Reports*, 5:11952, 2015.

[60] Jani Kotakoski, Christian Brand, Yigal Lilach, Ori Cheshnovsky, Clemens Mangler, Markus Arndt, and Jannik C. Meyer. Toward two-dimensional all-carbon heterostructures via ion beam patterning of single-layer graphene. *Nano Letters*, 15:5944–5949, 2015.

[61] Christopher J. Russo and J. A. Golovchenko. Atom-by-atom nucleation and growth of graphene nanopores. *Proceedings of the National Academy of Sciences of the United States of America*, 109:5953–5957, 2012.

[62] N. Toyoda and I. Yamada. Gas cluster ion beam equipment and applications for surface processing. *IEEE Transactions on Plasma Science*, 36:1471–1488, 2008.

[63] Songkil Kim, Anton V. Ievlev, Jacek Jakowski, Ivan V. Vlassiouk, Xiahan Sang, Chance Brown, Ondrej Dyck, Raymond R. Unocic, Sergei V. Kalinin, Alex Belianinov, Bobby G. Sumpter, Stephen Jesse, and Olga S. Ovchinnikova. Multi-purposed Ar gas cluster ion beam processing for graphene engineering. *Carbon*, 131:142–148, 2018.

[64] Bonnie J. Tyler, Barry Brennan, Helena Stec, Trupti Patel, Ling Hao, Ian S. Gilmore, and Andrew J. Pollard. Removal of organic contamination from graphene with a controllable mass-selected argon gas cluster ion beam. *Journal of Physical Chemistry C*, 119:17836–17841, 2015.

[65] Zabiholah Zabihi and Houshang Araghi. Formation of nanopore in a suspended graphene sheet with argon cluster bombardment: A molecular dynamics simulation study. *Nuclear Instruments and Methods in Physics Research Section B: Beam Interactions with Materials and Atoms*, 343:48–51, 2015.

[66] Shijun Zhao, Jianming Xue, Li Liang, Yugang Wang, and Sha Yan. Drilling nanopores in graphene with clusters: A molecular dynamics study. *Journal of Physical Chemistry C*, 116:11776–11782, 2012.

[67] Kichul Yoon, Ali Rahnamoun, Jacob L. Swett, Vighter Iberi, David A. Cullen, Ivan V. Vlassiouk, Alex Belianinov, Stephen Jesse, Xiahan Sang, Olga S. Ovchinnikovai, Adam J. Rondinone, Raymond R. Unocic, and Adri C.T. van Duin. Atomistic-scale simulations of defect formation in graphene under noble gas ion irradiation. *ACS Nano*, 10:8376–8384, 2016.

[68] Jennifer L. Achtyl, Raymond R. Unocic, Lijun Xu, Yu Cai, Muralikrishna Raju, Weiwei Zhang, Robert L. Sacci, Ivan V. Vlassiouk, Pasquale F. Fulvio, Panchapakesan Ganesh, David J. Wesolowski, Sheng Dai, Adri C. T. van Duin, Matthew Neurock, and Franz M. Geiger. Aqueous proton transfer across single-layer graphene. *Nature Communications*, 6:6539, 2015.

[69] F. Spath, J. Gebhardt, F. Dull, U. Bauer, P. Bachmann, C. Gleichweit, A. Gorling, H-P. Steinruck, and C. Papp. Hydrogenation and hydrogen intercalation of hexagonal boron nitride on Ni(111): Reactivity and electronic structure. *2D Materials*, 4:035026, 2017.

[70] Shaobin Tang and Zexing Cao. Structural and electronic properties of the fully hydrogenated boron nitride sheets and nanoribbons: Insight from first-principles calculations. *Chemical Physics Letters*, 488:67–72, 2010.

[71] S. Hu, M. Lozada-Hidalgo, F. C. Wang, A. Mishchenko, F. Schedin, R. R. Nair, E. W. Hill, D. W. Boukhvalov, M. I. Katsnelson, R. A. W. Dryfe, I. V. Grigorieva, H. A. Wu, and A. K. Geim. Proton transport through one-atom-thick crystals. *Nature*, 516:227–230, 2014.

[72] O. Leenaerts, B. Partoens, and F. M. Peeters. Graphene: A perfect nanoballoon. *Applied Physics Letters*, 93:193107, 2008.

[73] Wei Fang, Ji Chen, Yexin Feng, Xin-Zheng Li, and Angelos Michaelides. The quantum nature of hydrogen. *International Reviews in Physical Chemistry*, 38:35–61, 2019.

[74] Ronald A. Aziz. A highly accurate interatomic potential for argon. *Journal of Chemical Physics*, 99:4518–4525, 1993.

[75] A. A. Buchachenko, J. Jakowski, G. Chalasinski, M. M. Szczesniak, and S. M. Cybulski. *Ab initio* based study of the ArO^- photoelectron spectra: Selectivity of spin-orbit transitions. *Journal of Chemical Physics*, 112:5852–5865, 2000.

[76] J. Jakowski, G. Chalasinski, J. Gallegos, M. W. Severson, and M. M. Szczesniak. Characterization of Ar_nO^- clusters from *ab initio* and diffusion Monte Carlo calculations. *Journal of Chemical Physics*, 118:2748–2759, 2003.

[77] Michael Gaus, Qiang Cui, and Marcus Elstner. DFTB3: Extension of the self-consistent-charge density-functional tight-binding method (SCC-DFTB). *Journal of Chemical Theory and Computation*, 7:931–948, 2011.

[78] Yihan Shao, Zhengting Gan, Evgeny Epifanovsky, Andrew T. B. Gilbert, Michael Wormit, Joerg Kussmann, Adrian W. Lange, Andrew Behn, Jia Deng, Xintian Feng, Debashree Ghosh, Matthew Goldey, Paul R. Horn, Leif D. Jacobson, Ilya Kaliman, Rustam Z. Khaliullin, Tomasz Kuś, Arie Landau, Jie Liu, Emil I. Proynov, Young Min Rhee, Ryan M. Richard, Mary A. Rohrdanz, Ryan P. Steele, Eric J. Sundstrom, H. Lee Woodcock III, Paul M. Zimmerman, Dmitry Zuev, Ben Albrecht, Ethan Alguire, Brian Austin, Gregory J. O. Beran, Yves A. Bernard, Eric Berquist, Kai Brandhorst, Ksenia B. Bravaya, Shawn T. Brown, David Casanova, Chun-Min Chang, Yunqing Chen, Siu Hung Chien, Kristina D. Closser, Deborah L. Crittenden, Michael Diedenhofen, Robert A. DiStasio Jr., Hainam Do, Anthony D. Dutoi, Richard G. Edgar, Shervin Fatehi, Laszlo Fusti-Molnar, An Ghysels, Anna Golubeva-Zadorozhnaya, Joseph Gomes, Magnus W.D. Hanson-Heine, Philipp H.P. Harbach, Andreas W. Hauser, Edward G. Hohenstein, Zachary C. Holden, Thomas-C. Jagau, Hyunjun Ji, Benjamin Kaduk, Kirill Khistyaev, Jaehoon Kim, Jihan Kim, Rollin A. King, Phil Klunzinger, Dmytro Kosenkov, Tim Kowalczyk, Caroline M. Krauter, Ka Un Lao, Adèle D. Laurent, Keith V. Lawler, Sergey V. Levchenko, Ching Yeh Lin, Fenglai Liu, Ester Livshits, Rohini C. Lochan, Arne Luenser, Prashant Manohar, Samuel F. Manzer, Shan-Ping Mao, Narbe Mardirossian, Aleksandr V. Marenich, Simon A. Maurer, Nicholas J. Mayhall, Eric Neuscamman, C. Melania Oana, Roberto Olivares-Amaya, Darragh P. O'Neill, John A. Parkhill, Trilisa M. Perrine, Roberto Peverati, Alexander Prociuk, Dirk R. Rehn, Edina Rosta, Nicholas J. Russ, Shaama M. Sharada, Sandeep Sharma, David W. Small, Alexander Sodt, Tamar Stein, David Stück, Yu-Chuan Su, Alex J.W. Thom, Takashi Tsuchimochi, Vitalii Vanovschi, Leslie Vogt, Oleg Vydrov, Tao Wang, Mark A. Watson, Jan Wenzel, Alec White, Christopher F. Williams, Jun Yang, Sina Yeganeh, Shane R. Yost, Zhi-Qiang You, Igor Ying Zhang, Xing Zhang, Yan Zhao, Bernard R. Brooks, Garnet K.L. Chan, Daniel M. Chipman, Christopher J.

Cramer, William A. Goddard III, Mark S. Gordon, Warren J. Hehre, Andreas Klamt, Henry F. Schaefer III, Michael W. Schmidt, C. David Sherrill, Donald G. Truhlar, Arieh Warshel, Xin Xu, Alán Aspuru-Guzik, Roi Baer, Alexis T. Bell, Nicholas A. Besley, Jeng-Da Chai, Andreas Dreuw, Barry D. Dunietz, Thomas R. Furlani, Steven R. Gwaltney, Chao-Ping Hsu, Yousung Jung, Jing Kong, Daniel S. Lambrecht, WanZhen Liang, Christian Ochsenfeld, Vitaly A. Rassolov, Lyudmila V. Slipchenko, Joseph E. Subotnik, Troy Van Voorhis, John M. Herbert, Anna I. Krylov, Peter M.W. Gill, and Martin Head-Gordon. Advances in molecular quantum chemistry contained in the Q-Chem 4 program package. *Molecular Physics*, 113:184–215, 2015.

[79] M. Valiev, E. J. Bylaska, N. Govind, K. Kowalski, T. P. Straatsma, H. J. J. van Dam, D. Wang, J. Nieplocha, E. Apra, T. L. Windus, and W. A. de Jong. NWChem: A comprehensive and scalable open-source solution for large scale molecular simulations. *Computer Physics Communications*, 181:1477–1489, 2010.

[80] G. Ebel, R. Krohne, H. Meyer, U. Buck, R. Schinke, T. Seelemann, and P. Andresen. Rotationally inelastic scattering of NH_3 with H_2: Molecular-beam experiments and quantum calculations. *Journal of Chemical Physics*, 93:6419–6432, 1990.

[81] B. van Zyl, N. G. Utterback, and R. C. Amme. Generation of a fast atomic hydrogen beam. *Review of Scientific Instruments*, 47:814–819, 1976.

[82] H. Nakamura, A. Takayama, and A. Ito. Molecular dynamics simulation of hydrogen isotope injection into graphene. *Contributions to Plasma Physics*, 48:265–269, 2008.

[83] A. Ito and H. Nakamura. Molecular dynamics simulation of bombardment of hydrogen atoms on graphite surface. *Communications in Computational Physics*, 4:592–610, 2008.

[84] James F. Ziegler and Jochen P. Biersack. *Treatise on Heavy-Ion Science*, chapter The Stopping and Range of Ions in Matter. Springer, Boston, MA, 1985.

[85] James F. Ziegler, M. D. Ziegler, and J. P. Biersack. SRIM - the stopping and range of ions in matter (2010). *Nuclear Instruments and Methods in Physics Research Section B: Beam Interactions with Materials and Atoms*, 268:1818–1823, 2010. 19th International Conference on Ion Beam Analysis.

[86] L. Jeloaica and V. Sidis. DFT investigation of the adsorption of atomic hydrogen on a cluster-model graphite surface. *Chemical Physics Letters*, 300:157–162, 1999.

[87] Meng Miao, Marco Buongioro Nardelli, Qi Wang, and Yingchun Liu. First principles study of the permeability of graphene to hydrogen atoms. *Physical Chemistry Chemical Physics*, 15:16132–16137, 2013.

[88] L. Tsetseris and S. T. Pantelides. Graphene: An impermeable or selectively permeable membrane for atomic species? *Carbon*, 67:58–63, 2014.

[89] M. J. Knapp, K. Rickert, and J. P. Klinman. Temperature-dependent isotope effects in soybean lipoxygenase-1: Correlating hydrogen tunneling with protein dynamics. *Journal of the American Chemical Society*, 24:3865–3874, 2002.

[90] D. R. Killelea, V. L. Campbell, N. S. Shuman, and A. L. Utz. Bond-selective control of a heterogeneously catalyzed reaction. *Science*, 319:790–793, 2008.

[91] Niranji Thilini Ekanayake, Jingsong Huang, Jacek Jakowski, Bobby G. Sumpter, and Sophya Garashchuk. Relevance of the nuclear quantum effects on the proton/deuteron transmission through hexagonal boron nitride and graphene monolayers. *Journal of Physical Chemistry C*, 121:24335–24344, 2017.

[92] K. A. Mauritz and R. B. Moore. State of understanding of Nafion. *Chemical Reviews*, 104:4535–4585, 2004.

[93] W. L. Wang and E. Kaxiras. Graphene hydrate: Theoretical prediction of a new insulating form of graphene. *New Journal of Physics*, 12:125012, 2010.

[94] Q. Zhang, M. Ju, L. Chen, and X. C. Zeng. Differential permeability of proton isotopes through graphene and graphene analogue monolayer. *Journal of Physical Chemistry Letters*, 7:3395–3340, 2016.

[95] M. Seel and R. Pandey. Proton and hydrogen transport through two-dimensional monolayers. *2D Materials*, 3:025004, 2016.

[96] J. M. H. Kroes, A. Fasolino, and M. I. Katsnelson. Density functional based simulations of proton permeation of graphene and hexagonal boron nitride. *Physical Chemistry Chemical Physics*, 19:5813–5817, 2017.

[97] Y.-B. Xin, Q. Hu, D.-H. Niu, X.-H. Zheng, H.-L. Shi, M. Wang, Z.-S. Xiao, A.-P. Huang, and Z.-B. Zhang. Research progress of hydrogen tunneling in two-dimensional materials. *Acta Physica Sinica*, 66:056601, 2017.

[98] I. Poltavsky, L. Zheng, M. Mortazavi, and A. Tkatchenko. Quantum tunneling of thermal protons through pristine graphene. *Journal of Chemical Physics*, 148:204707, 2018.

[99] M. Lozada-Hidalgo, S. Hu, O. Marshall, A. Mishchenko, A. N. Grigorenko, R. A. W. Dryfe, B. Radha, I. V. Grigorieva, and A. K. Geim. Sieving hydrogen isotopes through two-dimensional crystals. *Science*, 351:68–70, 2016.

[100] R. Kosloff. Time-dependent quantum-mechanical methods for molecular dynamics. *Journal of Physical Chemistry*, 92:2087–2100, 1988.